



Studies of structural, dielectric and electrical properties of $\text{Bi}_4\text{Ti}_{2.9}\text{Sn}_{0.1}\text{O}_{12}$ electronic ceramic

N P SAMANTRAY* , B B ARYA, G DIGAL and R N P CHOUDHARY

Multifunctional Materials Research Laboratory, Department of Physics, Siksha 'O' Anusandhan (Deemed to be University), Bhubaneswar 751030, India

*Author for correspondence (npsamantray@gmail.com)

MS received 23 November 2022; accepted 20 July 2023

Abstract. In this paper, we have mainly reported the preliminary structural analysis and the frequency–temperature dependence of the dielectric and electrical properties of ceramic technology-fabricated Sn-modified bismuth titanate with a chemical composition of $\text{Bi}_4\text{Ti}_{2.9}\text{Sn}_{0.1}\text{O}_{12}$ electro-ceramic at room temperature. The compound is synthesized in a single-phase orthorhombic structure, as shown by the analysis of the X-ray diffraction pattern and data at room temperature. Detailed studies of dielectric and electrical properties in a wide temperature range (25 to 400°C) at different frequencies ranging from 1 to 1000 kHz have provided many important properties of the prepared sample. The dielectric constant and tangent loss at temperature 400°C and frequency 1 kHz are found to be 3×10^3 and 1.6, respectively. It was possible to calculate the contributions of the grains and grain boundaries to the overall resistance and capacitance of the synthesized material using Nyquist plots. The types of conduction mechanisms have been studied from an ac-conductivity study of the material. The J–E characteristics of the prepared sample which have slopes closer to 1, support the Ohmic behaviour. The study of the electric field and frequency dependence of electric polarization through hysteresis loops has confirmed the ferroelectric behaviour of the studied material at room temperature. Some experimental data obtained here suggest that the material may be useful as an electronic component in electronic industries.

Keywords. Solid-state reaction; ferroelectric; polarization; dielectric; impedance; conductivity.

1. Introduction

More attention is being placed on the synthesis of improved lead-free multifunctional materials due to their significant applications in sensors, transducers, energy harvesting devices, transformers, magnetic memory and spintronic devices [1,2]. Out of different multiferroic materials, bismuth titanate ($\text{Bi}_4\text{Ti}_3\text{O}_{12} = \text{BTO}$) has shown behaviours, such as ferroelectricity, photoconductivity and piezoelectricity [3,4]. Because of these properties, BTO has been proven to be an alternative to lead-containing multiferroics. The ferroelectric compound $\text{Bi}_4\text{Ti}_{2.9}\text{Sn}_{0.1}\text{O}_{12}$ has a layered structure and is a member of the Aurivillius family. It consists of $(\text{Bi}_2\text{O}_2)^{2+}$ slabs alternating with pseudo-perovskite layers $(\text{Bi}_2\text{Ti}_3\text{O}_{10})^{2-}$ arranged along the c-axis [5]. It has an orthorhombic structure with a high Curie temperature ($T_c = 675^\circ\text{C}$). BTO has a high dielectric constant, low dielectric loss and relatively low sintering temperature. A ferroelectric material for meaningful devices should have a lower coercive field, higher remnant polarization, low value of fatigue rate and low leakage current. But, pure $\text{Bi}_4\text{Ti}_3\text{O}_{12}$ suffers from some drawbacks, such as a high value of leakage current and low remnant polarization. To overcome these problems, a number of dopants, such as La,

Nd, Sm, Gd, Ru, Ba, Ce, Sn, Zr, etc., have been added. These additions have improved the phase stability and decreased oxygen defects of the compound [6]. It is also known that the volatilization nature of bismuth can produce oxygen vacancies during the sintering process of BTO. However, the microwave sintering (MWS) approach can lower the volatilization of Bi and can reduce the oxygen vacancy and improve the relaxation behaviour of ferroelectric materials [7]. Other than suitable substitution or addition of appropriate elements at different atomic sites of the materials, the selection of synthesis methods and experimental conditions are also useful to improve their properties. There are several methods, such as solid-state reaction, high energy ball milling, sol–gel, sol–gel auto combustion, oxalate precursor, co-precipitation method, etc., which are frequently used to synthesize the materials. Each one has its advantages and disadvantages. Though some of the above chemical methods provide accuracy in stoichiometric ratio, compositional homogeneity and low crystallization temperature [8], the solid-state reaction or oxide method is found to be user-friendly and cost-effective. Because of these, we have employed a solid-state reaction route to synthesize the following proposed material. Knowing the importance of the material and

unavailability of detailed dielectric, ferroelectric and electrical data of Sn-modified $\text{Bi}_4\text{Ti}_3\text{O}_{12}$, we have synthesized it by the addition of 10% Sn with a general chemical composition of $\text{Bi}_4\text{Ti}_{2.9}\text{Sn}_{0.1}\text{O}_{12}$. In this communication, structural, dielectric and electrical properties of $\text{Bi}_4\text{Ti}_{2.9}\text{Sn}_{0.1}\text{O}_{12}$ electro-ceramics have been presented briefly.

2. Experimental

$\text{Bi}_4\text{Ti}_{2.9}\text{Sn}_{0.1}\text{O}_{12}$ was synthesized by a mixed oxide technique at a temperature of 850°C by using high-quality analytical grade (purity $> 99.9\%$) oxides, such as bismuth oxide (Bi_2O_3), titanium dioxide (TiO_2) and stannic oxide (SnO_2) procured from the M/S Loba Chemie Co. Pvt. Ltd. All these ingredients were homogeneously mixed in proper stoichiometric ratio and ground for 4 h in the open air before mixing with methanol for another 4 h. Then, using a cylindrical alumina crucible (M/S ANTS ceramics), the produced sample was heated at various temperatures before being heated at 850°C for 5 h. The calcinated sample was finely powdered and mixed uniformly with one or two drops of PVA solution for better binding during the preparation of circular pellets. These pellets had a diameter of about 1.2 cm and a thickness ranging from 0.1 to 0.2 cm and they are formed using a KBr press (M/S Techno Search Instruments Co.) at a hydraulic pressure of $4 \times 10^6 \text{ N m}^{-2}$. Then the pellets were sintered at 850°C for 6 h. The calcined powder of $\text{Bi}_4\text{Ti}_{2.9}\text{Sn}_{0.1}\text{O}_{12}$ was utilized for the structural investigation to get the crystal data using an X-ray diffractometer (Rigaku, Japan) having Cu $K\alpha$ radiation (λ) of 1.5405 Å. High-quality silver paint was applied to the polished surfaces of the sintered pellets to make electrodes for different measurements. Before taking electrical measurements, the pellets were reheated at a temperature of 120°C for 2 h to remove any moisture. The phase-sensitive meter (N4L model PSM 1735) was used for recording various electrical and dielectric measurements. The measurements were recorded within the frequency range of 1 kHz to 1 MHz and temperature range of 25 to 400°C . P-E loop tracers (Marine India) were used to trace the hysteresis loops of the sample at room temperature by varying the applied electric field. The leakage current characteristics of the materials were examined using a programmable electrometer (Keithley, model 6517B).

3. Results and discussions

3.1 Structural study

The X-ray diffraction (XRD) spectrum of the polycrystalline powder sample ($\text{Bi}_4\text{Ti}_{2.9}\text{Sn}_{0.1}\text{O}_{12}$) prepared at room temperature is depicted in figure 1a. The preliminary structural analysis was performed by analysing the XRD pattern and data recorded in a wide range of twice the

diffraction angle varying from 20° to 80° . All the major peaks show the fundamental XRD data/pattern, different from those of the ingredients used, which confirms that a new single-phase compound is formed. All the prominent peaks were indexed by using the JCPDS database of bismuth titanium oxide ($\text{Bi}_4\text{Ti}_3\text{O}_{12}$) (ICSD card number 01-089-7500). The compound is crystallized in the orthorhombic crystal system, with standard unit cell parameters: $a = 5.4444 \text{ \AA}$, $b = 5.4086 \text{ \AA}$, $c = 32.8425 \text{ \AA}$, $\alpha = \beta = \gamma = 90^\circ$ with cell volume (V) = $967.10 (\text{Å})^3$ and density 8.05 g cm^{-3} .

The comparison of observed data (Y_{obs}) with the calculated data (Y_{cal}) of the XRD spectrum is made by using the computer software MAUD and is presented in figure 1b. The X-ray diffraction pattern was refined by comparing the observed and calculated peaks with the crystallographic information file from the crystallographic open database (i.e., COD: 1528445) of the orthorhombic-structured BTO. The quality (validity) of refinement is expressed by the difference between the observed data (black solid symbol) and calculated data (red solid line) is shown by a blue solid line. The lattice constants of the synthesized sample from Rietveld refinement are found to be $a = 32.8683 \text{ \AA}$, $b = 5.4148 \text{ \AA}$ and $c = 5.4507 \text{ \AA}$, which have been used to index all the peaks of the XRD pattern (figure 1a). It is observed that the unit cell dimensions obtained in the present analysis are quite comparable and identical with the reported one (Rietveld analysis) except for the interchange in the a and c unit cell dimensions.

The quality (accuracy) of the Rietveld refinement is normally given by the reliability parameters (R -values), i.e., R_w (weighted profile residual factor), R_b (Bragg R factor), R_{exp} (expected residual factor) and σ (the goodness of fit). The obtained R -values are given in figure 1b.

A perfect crystal would extend in all directions to infinity, so no crystals are perfect due to their finite size. As a result of this divergence from perfect crystallinity, there is a broadening of the diffraction peaks. The two main properties extracted from peak width analysis are: (a) crystallite size and (b) lattice strain. Crystallite size is an indicator of coherent diffracting domain size. Lattice strain is a measure of the distribution of lattice constants arising from crystal imperfections and distortion [9].

The crystallite size of the sample can be calculated by the Scherrer equation [10] as given below:

$$P = \frac{k\lambda}{\beta \cos \theta} \quad (1)$$

where k is the dimensionless shape factor constant with a value of 0.94 for orthorhombic unit cell, $\lambda = 1.5406 \text{ \AA}$ representing the wavelength of Cu $K\alpha$ radiation, β the full width at half maxima (FWHM) and θ the Bragg's diffraction angle of the considered peak. Using the above formula, the average crystallite size of the material is calculated to be 37 nm.

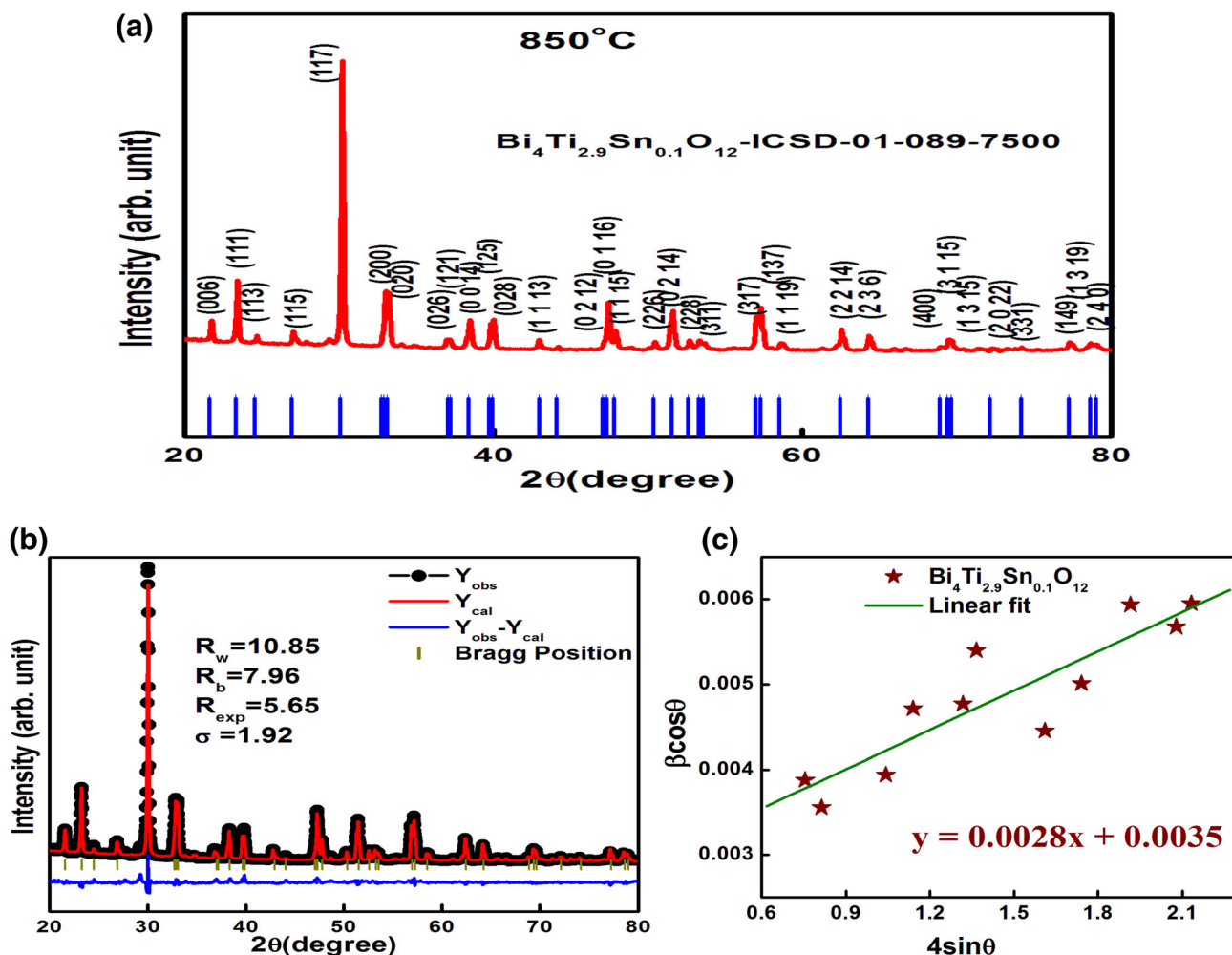


Figure 1. (a) XRD pattern, (b) Rietveld refinement results and (c) Williamson–Hall plot of $\text{Bi}_4\text{Ti}_{2.9}\text{Sn}_{0.1}\text{O}_{12}$.

Williamson–Hall (W–H) analysis is a simplified integral breadth method where both size-induced and strain-induced broadening are evaluated by considering the peak width as a function of 2θ [11]. The strain induced in powders due to crystal imperfection and distortion was calculated using the formula:

$$\varepsilon = \frac{\beta}{4 \tan \theta} \quad (2)$$

As the contributions of crystallite or particle size and strain to line broadening are independent of each other, they can follow a Cauchy-like relation. Hence, the observed line breadth is simply the sum of equations (1 and 2). Hence,

$$\beta = \frac{k\lambda}{P \cos \theta} + 4\varepsilon \tan \theta$$

Rearranging the above equation, we get

$$\beta \cos \theta = \frac{k\lambda}{P} + 4\varepsilon \sin \theta \quad (3)$$

Equation (3) is the Williamson–Hall (W–H) equation. The crystallite size (P) and lattice strain (ε) of the material can

be determined from the intercept and the slope, respectively, of the linear fitting line on the $\beta \cos \theta$ vs. $4 \sin \theta$ graph, which is known as Williamson–Hall plot and shown in figure 1c. The mean value of crystallite size and the lattice strain are observed to be 37.6 nm and 0.0028, respectively. The crystallite size determined by using the Scherrer equation and Williamson–Hall plot is very much comparable to each other. Positive lattice strain suggests the presence of tensile strain in the crystal system [12].

3.2 Dielectric study

All the information about different polarizations, relaxation processes, causes of dielectric loss, etc., can be obtained from the dielectric study [13,14]. The dielectric specimen gets polarized by applying an ac field. Because of polarization, the dielectric parameters of the specimen get changed. The electrical polarization and temporal phase shift produced in the driving force cause a decrease in the current component in the prepared sample. Hence, the

dielectric loss in the sample is due to this decrease in the current component.

The variation of the dielectric parameters (relative dielectric constant and dielectric/tangent loss) of $\text{Bi}_4\text{Ti}_{2.9}\text{Sn}_{0.1}\text{O}_{12}$ with frequency (1 to 1000 kHz) within a temperature range from 25 to 400°C is shown in figure 2a and b. The analysis of dielectric parameters provide details about the different types of polarization, relaxation processes, defects, dielectric loss, etc., of the sample. Dielectric properties show a consistent variation with temperature and frequency changes. With increasing frequency, it can be observed that both the tangent loss ($\tan \delta$) and the dielectric constant (ϵ_r) are decreasing. The dielectric dispersion of the spectrum of the dielectric constant at low frequencies confirms the dielectric and ferroelectric behaviour of the synthesized material [15–17]. Polarization, oxygen vacancies, the grain boundary effect, phase composition, doping concentration and interfacial dislocations are all factors that contribute to the higher value of the dielectric constant at low frequencies [18,19]. The existence of various

polarization processes, including dipolar, ionic, atomic, space charge and electronic polarization, mainly accounts for the high dielectric constant in the low-frequency region. The small displacement produced due to these polarizations is the cause of the net polarization of the material [13]. Out of all these polarizations, electronic polarization and the ferroelectric region have major contributions to relative permittivity at high frequencies. Hence, for higher frequencies ($>10^4$ Hz), there is a decrease in the value of the dielectric constant with an increase in frequency. Again, the tangent loss typically rises for a low-frequency ac signal due to an increase in resistance of grain boundaries and falls with frequency. Based on Koop's phenomenological theory, the Maxwell and Wagner effect may explain such type of fluctuations in dielectric properties [20].

The variation of the relative dielectric constant of $\text{Bi}_4\text{Ti}_{2.9}\text{Sn}_{0.1}\text{O}_{12}$ electro-ceramics with temperature is shown in figure 2c. As observed for a particular frequency, relative permittivity (ϵ_r) increases with a rise in temperature at all studied frequencies. The temperature for which

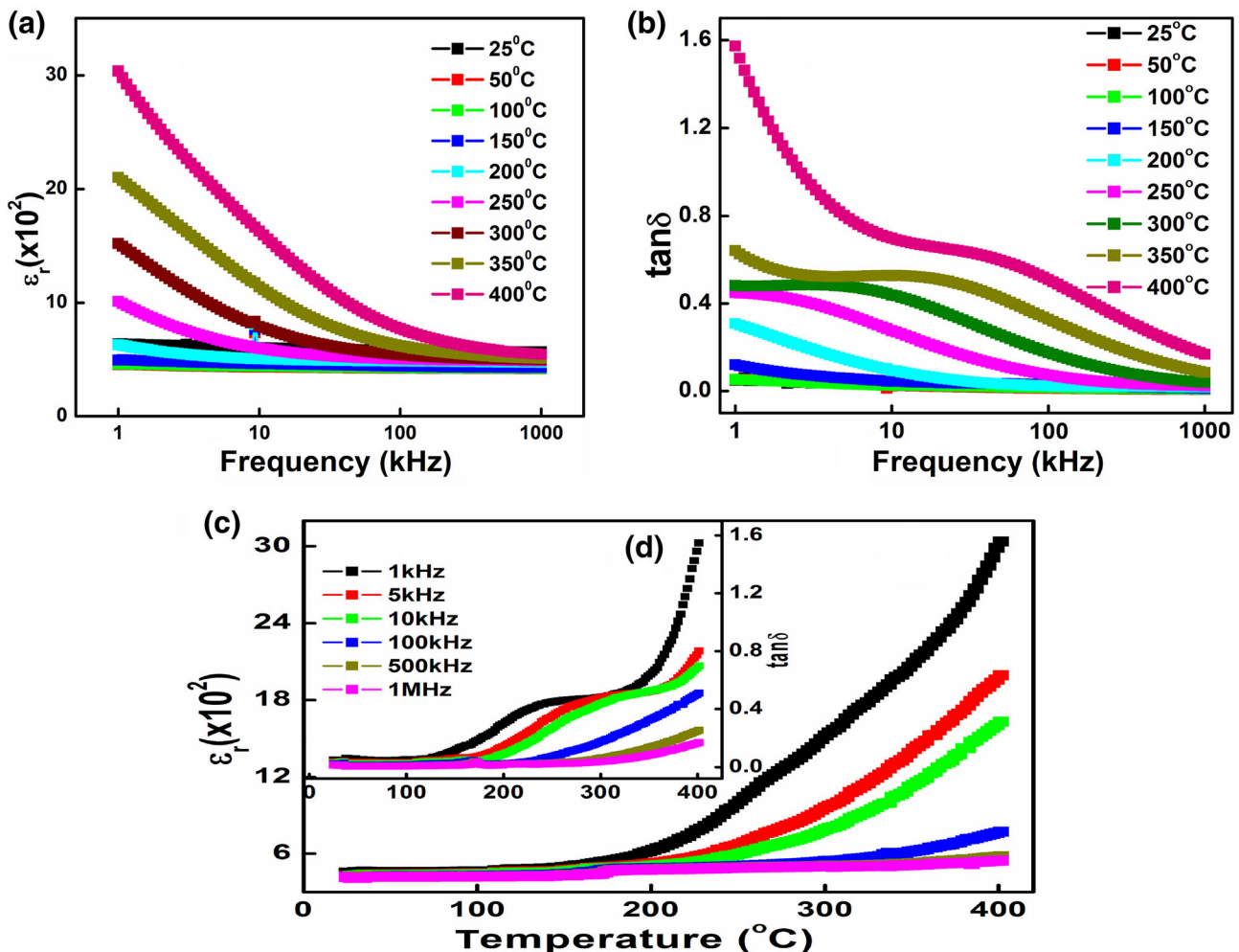


Figure 2. (a) Variation of relative dielectric constant with the frequency of $\text{Bi}_4\text{Ti}_{2.9}\text{Sn}_{0.1}\text{O}_{12}$. (b) Variation of tangent loss ($\tan \delta$) with the frequency of $\text{Bi}_4\text{Ti}_{2.9}\text{Sn}_{0.1}\text{O}_{12}$. (c, d) Variation of dielectric parameters with the temperature of $\text{Bi}_4\text{Ti}_{2.9}\text{Sn}_{0.1}\text{O}_{12}$.

permittivity or dielectric constant becomes maximum is known as Curie temperature (T_c) [21]. However, in the analysed temperature range, we are unable to observe any dielectric anomalies or phase transitions in the sample, as the transition temperature of the parent compound is much above the studied temperature range. A similar trend is observed in the study of temperature-dependent tangent loss except for some relaxation wide peaks in the given frequencies 1, 5 and 10 kHz (figure 2b, d (inset)). This broadening in peak is observed between temperatures from 200 to 300°C and shifted to a higher temperature side on increasing the frequency. This broadening in peak may be due to space charge polarization [22]. Again, the increase in $\tan \delta$ with an increase in temperature is because of defects, such as oxygen vacancies, thermally induced increase in the motion of charge carriers and the presence of an impurity phase in the synthesized sample [23].

3.3 Impedance study

The complex impedance spectroscopy (CIS) technique is used to study the impedance of multiferroic samples [24]. The CIS technique may be used to investigate the impact of grains and grain boundaries on dielectrics. Figure 3a and b depict the fluctuation of impedance characteristics, namely, the real component (Z') and imaginary component (Z''), as a function of the frequency of the prepared sample $\text{Bi}_4\text{Ti}_{2.9}\text{Sn}_{0.1}\text{O}_{12}$. In the figures, it is shown that as temperature increases, Z' decreases in the low-frequency region (1 to 100 kHz). At frequencies higher than 100 kHz, Z' merges with itself. This kind of impedance spectrum is caused by the discharge of space charges. The sample's negative temperature coefficient of resistance (NTCR) behaviour is again confirmed by the decrease in the Z' value that occurs when temperature increases in the low-frequency band [25]. The variation of Z'' with frequency (1 to 1000 kHz) at selected temperatures (25 to 400°C) is depicted in figure 3b. The plot also shows that with an increase in frequency, Z'' goes on decreasing and the spectrum tends to combine at higher frequencies.

The Nyquist plot shows the variation of real component (Z') with imaginary component (Z'') of complex impedance at different temperatures in the range of 25 to 400°C (figure 3c). The semicircular arcs (one or more than one) determine the resistive behaviour of the sample. An ideal semicircular arc with its origin on the real Z -axis is required for a Debye-type relaxation. But, the non-Debye type of relaxation phenomena in the prepared samples is confirmed by the degree of depressions in the semicircular arcs. Two semicircles can be used in Nyquist plots to represent the grains and grain boundaries of the sample. The sample is extremely insulating, as seen by the nearly straight lines with a large slope at low temperatures. The curves bend toward the actual Z' -axis as the temperature increases, forming deformed semicircular arcs. The radius of the

deformed semicircular arc decreases as the temperature rises, demonstrating that resistance decreases as temperature increases. It is observed that the respective capacitance values of grain boundaries and grains are the same [26]. The study of Nyquist plots using ZSimpWin software [27] reveals that all the curves from 25 to 200°C are fitted by a single semicircular arc with parallel RQC circuits indicating the grain effect. The curves from 250 to 400°C are represented by overlapping semicircular arcs fitted with a parallel RQC along with a parallel RC circuit representing the grains and grain boundaries. The resistance, capacitance and constant phase of the grains and their boundaries are listed in table 1. The depressed semicircular arc of the sample at 200°C is shown in figure 3d, with the depression angle (θ_g) equal to 8.12°.

3.4 Electrical conductivity study

The frequency dependence ac-conductivity for the sample $\text{Bi}_4\text{Ti}_{2.9}\text{Sn}_{0.1}\text{O}_{12}$ with frequency (1–1000 kHz) at constant temperatures (25 to 400°C) is plotted in figure 4a. The expression for ac-conductivity is given by

$$\sigma_{ac}(\omega) = \sigma_x + P\omega^\eta \quad (4)$$

This formula is known as the Jonscher's power law [28]. Here, σ_x is the frequency-independent dc-conductivity component, P the temperature-dependent polarizability component and η the exponent of a power-law. The value of the exponent η which ranges from 0 to 1, represents the interaction of mobile ions with the crystal lattice. The conductivity vs. frequency spectrum depicts that the ac-conductivity increases as the frequency increases. The negative temperature coefficient of resistance (NTCR) behaviour of the synthesized sample may be validated because ac-conductivity increases with an increase in frequency and temperature.

The variation in ac-conductivity of $\text{Bi}_4\text{Ti}_{2.9}\text{Sn}_{0.1}\text{O}_{12}$ with the inverse of absolute temperature at various frequencies can be studied in figure 4b. The plots confirm the increase in $\log \sigma_{ac}$ with the rise in absolute temperature. The ac-conductivity may be calculated by using the formula:

$$\sigma_{ac} = \sigma_0 \exp\left(-\frac{E_a}{kT}\right) \quad (5)$$

where k and σ_0 are the Boltzmann constant and the pre-exponential factor, respectively. The activation energy E_a can be determined by using linear fittings. Multiple conduction with varying activation energies occur in the synthesized sample, as represented by the existence of different slopes at various temperature ranges.

In higher temperature regions, the value of σ_{ac} increases sharply on increasing the temperature. This suggests that the plots are Arrhenius type. In lower temperature regions, it is found that for a given frequency, the value of σ_{ac} increases with an increase in temperature. The cause of an increase in

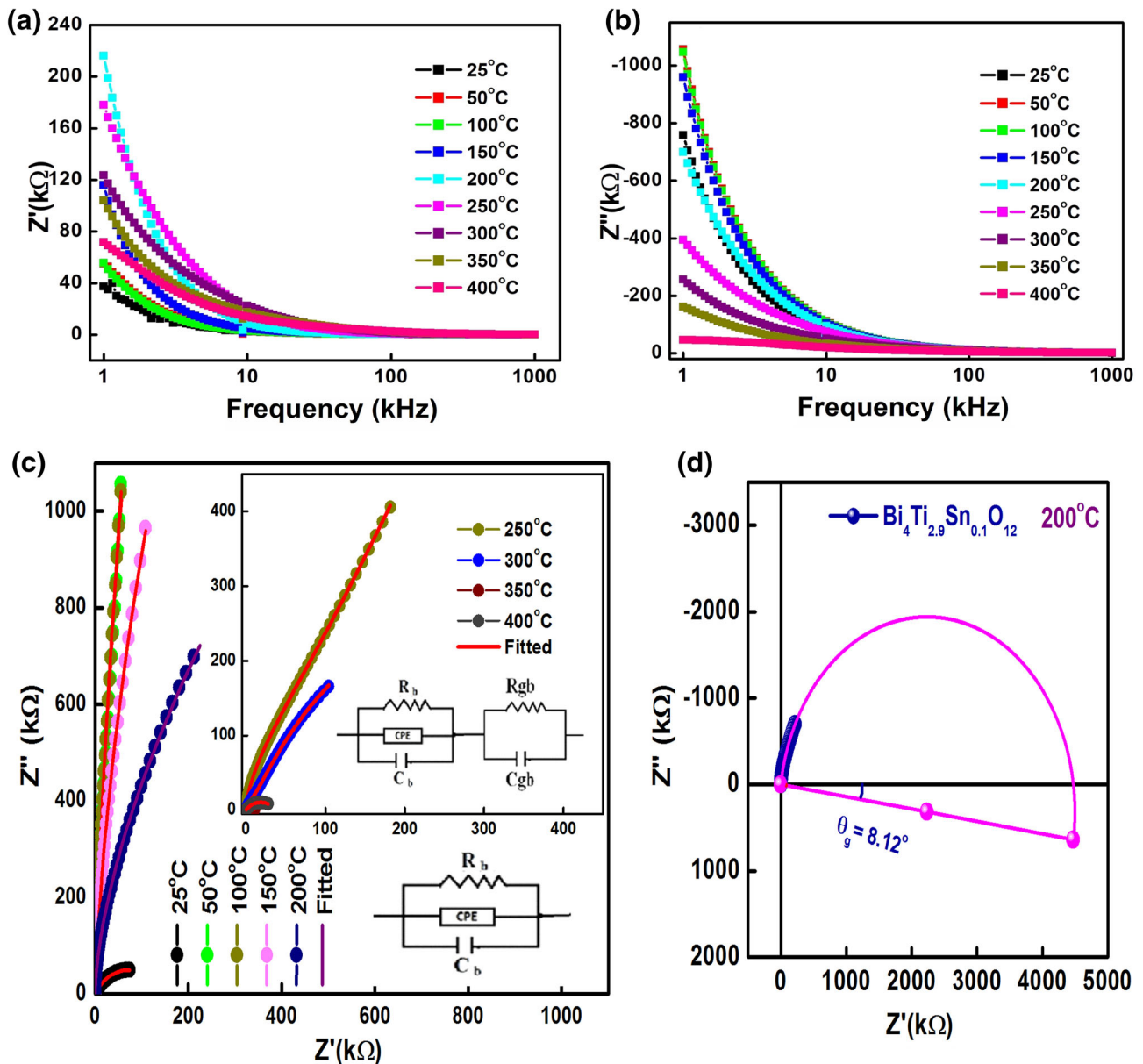


Figure 3. (a) Variation of Z' with the frequency of $\text{Bi}_4\text{Ti}_{2.9}\text{Sn}_{0.1}\text{O}_{12}$. (b) Variation of Z'' with the frequency of $\text{Bi}_4\text{Ti}_{2.9}\text{Sn}_{0.1}\text{O}_{12}$. (c) Nyquist plot of $\text{Bi}_4\text{Ti}_{2.9}\text{Sn}_{0.1}\text{O}_{12}$. (d) Depressed semicircle at 200°C of $\text{Bi}_4\text{Ti}_{2.9}\text{Sn}_{0.1}\text{O}_{12}$.

σ_{ac} is due to the increase in mobility of charge carriers with an increase in temperature, which in turn increases the conductivity of the sample [29]. This results in the hopping of charge carriers, which confirms the semiconductor behaviour of $\text{Bi}_4\text{Ti}_{2.9}\text{Sn}_{0.1}\text{O}_{12}$, which has a negative temperature coefficient of resistance (NTCR). Using linear fitting, it is also estimated that the values of activation energy in $\text{Bi}_4\text{Ti}_{2.9}\text{Sn}_{0.1}\text{O}_{12}$ are higher at lower frequencies. At frequencies of 1 kHz and 1 MHz, the activation energies are determined to be 0.99777 and 0.48663 eV, respectively. The higher value of E_a of the material at lower frequencies may be due to a strong long-range mobility of charge carriers [30].

3.5 Modulus analysis

The variations in the real part of the electrical modulus (M') with frequency at constant temperatures for $\text{Bi}_4\text{Ti}_{2.9}\text{Sn}_{0.1}\text{O}_{12}$ are depicted in figure 5a. For lower frequency regions and temperatures, M' have smaller values which indicate the major contribution of electrode polarization. Again, at lower frequencies, the collection of space charges takes place near the interface. The lack of the restoring force for the mobility of charge carriers caused by the induced electric field is once again confirmed by the continuous increase in M' with frequency for constant temperatures [31]. Additionally, the fact that M' increases as frequency

Table 1. Resistance and capacitance of grains (R_g and C_g) and grain boundaries (R_{gb} and C_{gb}) of $\text{Bi}_4\text{Ti}_{2.9}\text{Sn}_{0.1}\text{O}_{12}$.

Temp. ($^{\circ}\text{C}$)	Model	R_b (Ω)	CPE	C_b (F)	R_{gb} (Ω)	C_{gb} (F)
25	(RQC)	1.481×10^8	1.769×10^{-10}	1.775×10^{-10}		
50	(RQC)	2.063×10^8	2.337×10^{-10}	1.364×10^{-10}		
100	(RQC)	1.681×10^7	1.573×10^{-10}	1.324×10^{-10}		
150	(RQC)	1.681×10^7	1.573×10^{-10}	1.324×10^{-10}		
200	(RQC)	1.666×10^{13}	1.604×10^{-8}	1.570×10^{-10}		
250	(RQC)(RC)	6.472×10^{12}	2.542×10^{-5}	2.170×10^{-10}	2.827×10^6	6.052×10^{-10}
300	(RQC)(RC)	8.322×10^{14}	1.201×10^{-5}	1.975×10^{-10}	4.426×10^5	1.074×10^{-9}
350	(RQC)(RC)	8.322×10^{14}	1.201×10^{-5}	1.975×10^{-10}	4.426×10^5	1.074×10^{-9}
400	(RQC)(RC)	3.627×10^4	5.153×10^{-8}	1.866×10^{-10}	7.677×10^2	1.326×10^{-9}

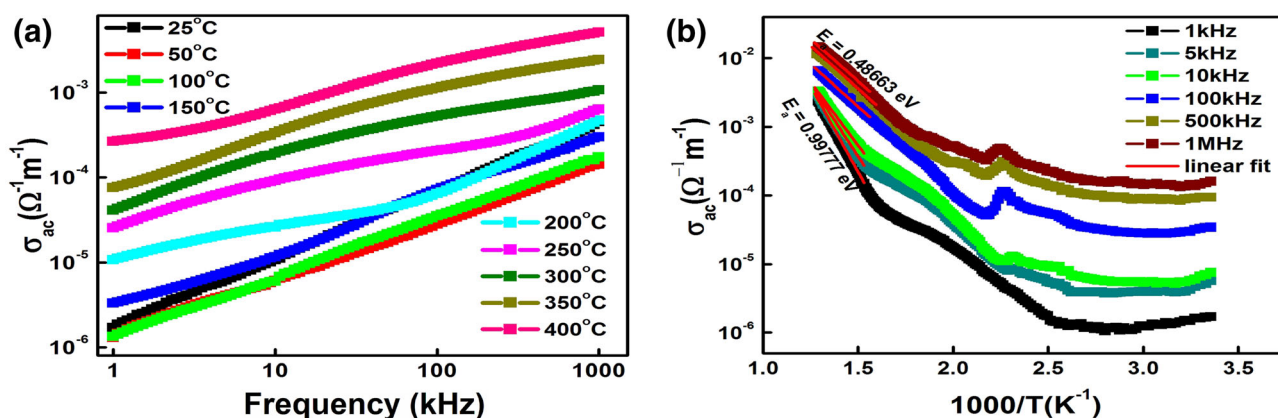


Figure 4. (a) Variation in ac-conductivity with frequency of $\text{Bi}_4\text{Ti}_{2.9}\text{Sn}_{0.1}\text{O}_{12}$. (b) Variation in ac-conductivity with inverse absolute temperature of $\text{Bi}_4\text{Ti}_{2.9}\text{Sn}_{0.1}\text{O}_{12}$.

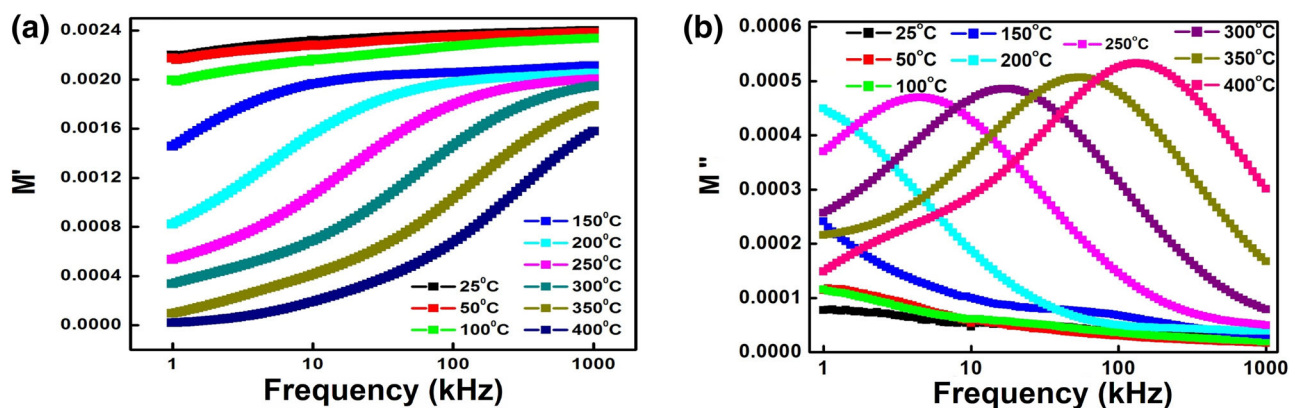


Figure 5. (a) Variation of M' with the frequency of $\text{Bi}_4\text{Ti}_{2.9}\text{Sn}_{0.1}\text{O}_{12}$. (b) Variation of M'' with the frequency of $\text{Bi}_4\text{Ti}_{2.9}\text{Sn}_{0.1}\text{O}_{12}$.

increases supports the relaxation phenomenon driven by the short-range mobility of the charge carriers. This might be noticed for a wide range of frequencies.

The dependence of the imaginary component of the electrical modulus (M'') with frequency is depicted in

figure 5b. The peaks in the curves are caused by the switching of the charge carriers from short-range to long-range mobility as the frequency changes. Again, charge carriers migrate to higher frequency areas inside the potential well [32].

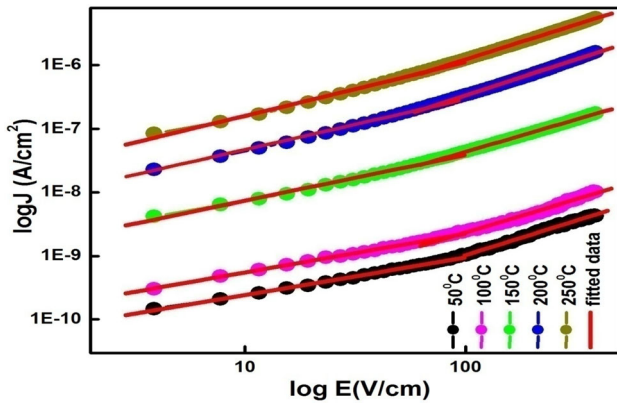


Figure 6. Variation of $\log J$ vs. $\log E$ for $\text{Bi}_4\text{Ti}_{2.9}\text{Sn}_{0.1}\text{O}_{12}$.

3.6 J - E characteristics

To analyse the conduction mechanism of the samples, J - E characteristics are necessary. Figure 6 shows the variation of $\log J$ with $\log E$ within the temperature range 50 to 250°C. According to the plot of $\log J$ vs. $\log E$, the current density changes linearly with the applied electric field in both lower and higher voltage regions. The slopes for temperatures 50, 100, 150, 200 and 250°C in lower electric field regions are found to be 0.61060, 0.61340, 0.71866, 0.79621 and 0.84427, respectively. For higher electric fields, the slopes are 1.0887, 1.0414, 1.0168, 1.1278 and 1.0965, respectively. Using linear fit, slopes are found to be closer to 1 and the Ohmic conduction for lower voltage region is confirmed due to the electrons, which are stimulated thermally.

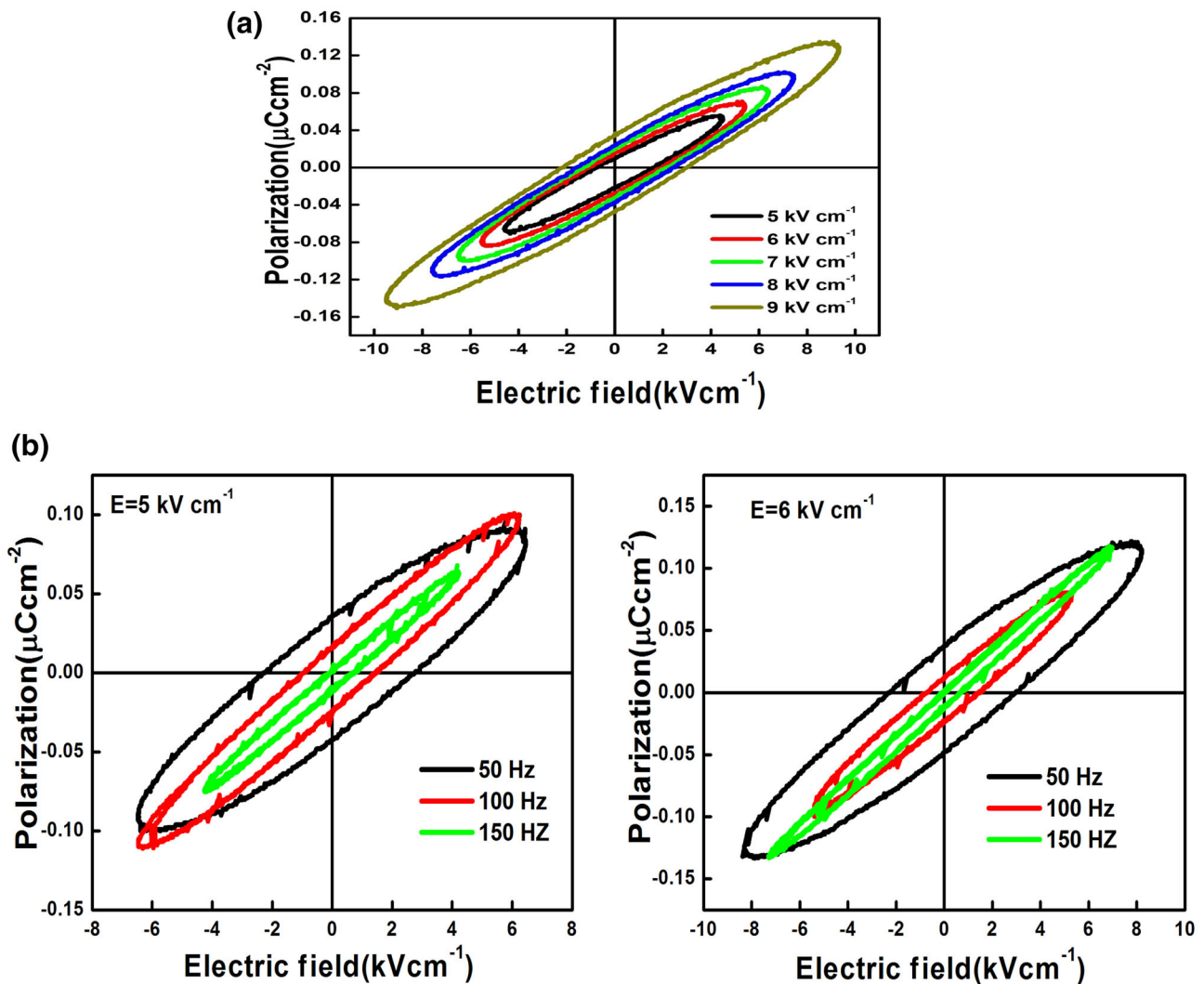


Figure 7. (a) Field dependence of P - E hysteresis loops for $\text{Bi}_4\text{Ti}_{2.9}\text{Sn}_{0.1}\text{O}_{12}$. (b) Variation of P - E hysteresis loops for $\text{Bi}_4\text{Ti}_{2.9}\text{Sn}_{0.1}\text{O}_{12}$ at different frequencies.

The electric current density J of the sample is given by the equation:

$$J = ne\mu\frac{v}{d} = \sigma\frac{v}{d} = \sigma E \quad (6)$$

where n denotes the density of free charge carriers, e the charge of an electron, μ the mobility of free carriers in the transport band, V the applied voltage, d the sample thickness, σ the electrical conductivity and E the applied electric field [33].

3.7 Ferroelectricity

The electric field-dependent polarization (P–E) hysteresis loops of the synthesized sample $\text{Bi}_4\text{Ti}_{2.9}\text{Sn}_{0.1}\text{O}_{12}$ at room temperature (frequency = 50 Hz) are shown in figure 7a. The measurements are taken by varying the applied electric field from 1 to 5 kV cm^{-1} across the sample. The coercive field, residual polarization, and size of the loop are characteristics of ferroelectricity [34]. The nature of the hysteresis loops confirms the ferroelectric behaviour of the prepared material at room temperature. Because of the small leakage current, the hysteresis loops are not smooth. Again, it is found that the remnant polarization, coercive field and the area of the loops increase with an increase in the applied electric field. The value of remnant polarization ($2P_r$) and coercive field ($2E_c$) at 5 kV cm^{-1} are observed to be 0.032 $\mu\text{C cm}^{-1}$ and 2.4 kV cm^{-1} , respectively, whereas at 9 kV cm^{-1} these values are increased to 0.083 $\mu\text{C cm}^{-1}$ and 5.19 kV cm^{-1} , respectively.

Figure 7b shows hysteresis loops for $\text{Bi}_4\text{Ti}_{2.9}\text{Sn}_{0.1}\text{O}_{12}$ electro-ceramics measured at various frequencies for constant applied fields (E) of 5 and 6 kV cm^{-1} . The remnant polarization ($2P_r$) and the coercive field ($2E_c$) of $\text{Bi}_4\text{Ti}_{2.9}\text{Sn}_{0.1}\text{O}_{12}$ ceramics decreases as the frequency increases. It is due to the oxygen vacancy in the sample, which causes space charge polarization, turning direction polarization, and electron and ion displacement polarization [35]. As the frequency rises from 50 to 150 Hz, the space charge polarization is unable to keep up with the shift in the electric field, which causes the remnant polarization and coercive field to fall.

4. Conclusions

The electro-ceramics $\text{Bi}_4\text{Ti}_{2.9}\text{Sn}_{0.1}\text{O}_{12}$ was synthesized by the mixed oxide reaction process at 850°C. Both XRD spectral analysis and Rietveld refinement confirm that the sample is formed in an orthorhombic crystal system. The study of variations of dielectric constant (ϵ_r) as well as tangent loss ($\tan \delta$) with frequency is explained by the Maxwell and Wagner effect and confirms the dielectric properties of the synthesized sample. The NTCR behaviour of the sample is confirmed by the impedance analysis, and

the relaxation phenomena, which is not of the Debye-type, is confirmed by the Nyquist plot. The P–E hysteresis loops prove the existence of ferroelectric behaviour at room temperature, and the remnant polarization falls with a rise in frequency. The Ohmic conduction mechanism was confirmed by J–E characteristics as the slopes are closer to 1. Because of the higher dielectric constant, lower tangent loss, and smaller leakage current, this material is very useful for various multifunctional electronic devices.

References

- [1] Gajek M, Fusil S, Bouzehouane K, Fontcuberta J, Barthelémy A, Fert A *et al* 2007 *Nat. Mater.* **6** 296
- [2] Bibes M and Barthélémey A 2008 *Nat. Mater.* **7** 425
- [3] Subohi O, Kumar G S, Malik M M and Kurchania R 2012 *Phys. B: Condens. Matter* **407** 3813
- [4] Chen H, Shen B, Xu J and Zhai J 2013 *J. Alloys Compd.* **551** 92
- [5] Hou D, Luo W, Huang Y, Yu J C and Hu X 2013 *Nanoscale* **5** 2028
- [6] Cai W, Gao R L, Yao L W, Chen G, Deng X L, Wang Z H *et al* 2019 *J. Alloys Compd.* **774** 61
- [7] Fan Tao, Ji Cong, Chen Gang, Cai Wei, Gao Rongli, Deng Xiaoling *et al* 2020 *Mater. Chem. Phys* **250** 123034
- [8] Qianwei Zhang, Cai W, Qingting Li, Gao R L, Chen G, Deng X L *et al* 2019 *J. Alloys Compd.* **794** 542
- [9] Mote V D, Purushotham Y and Dole B N 2012 *J. Theor. Appl. Phys.* **6** 6
- [10] Purohit V, Padhee R and Choudhary R N P 2018 *Ceram. Int.* **44** 3993
- [11] Suryanarayana C and Grant Norton M 1998 X-ray diffraction: A practical approach. Springer, New York
- [12] Kumar Nitin, Shukla Alok and Choudhary R N P 2017 *Phys. Lett.A* **381** 2721 <https://doi.org/10.1016/j.physleta.2017.06.012>
- [13] Pattanayak S, Choudhary R N P, Das P R and Shannigrahi S R 2014 *Ceram. Int.* **40** 7983
- [14] Tang M, Jiang B, Zhang W, Xiao Y, Zhou Y, He J *et al* 2012 *Thin Solid Films* **520** 6684
- [15] Anderson J C 1964 *Dielectrics* (London: Chapman & Hall)
- [16] Gao R L, Zhang Qingmei, Zhiyi Xu, Wang Zhenhua, Chen Gang, Deng Xiaoling *et al* 2019 *Compos. B Eng.* **166** 204
- [17] Gao R L, Xiaofeng Qin, Qingmei Zhang, Zhiyi Xu, Zhenhua Wang, Chunlin Fu *et al* 2019 *J. Alloys Compd.* **795** 501
- [18] Troyanchuk I O, Trukhanov S V, Khalyavin D D and Szymczak H 2000 *J. Magn. Magn. Mater.* **208** 217
- [19] Gao R L, Wang Z H, Chen G, Deng X L, Cai W and Fu C L 2018 *Ceram. Int.* **44** S84
- [20] Pawar R P and Puri V 2014 *Ceram. Int.* **40** 10423
- [21] Shlimas D I, Zdorovets M V and Kozlovskiy A L 2020 *J. Mater. Sci.: Mater. Electron.* **31** 12903
- [22] Barick B K, Mishra K K, Arora A K, Choudhary R N P and Dillip K Pradhan 2011 *J. Phys. D: Appl. Phys.* **44** 355402
- [23] Sen S and Choudhary R N P 2004 *Mater. Chem. Phys.* **87** 256

- [24] Macdonald J R and Johnson W B 2005 *Impedance Spectroscopy Theory, Experiments and Applications* (Hoboken: Wiley)
- [25] Pattanayak S, Parida B N, Das P R and Choudhary R N P 2013 *Appl. Phys. A* **112** 387
- [26] Rehman Fida, Li Jing-Bo, Zhang Jia-Song, Rizwan Muhammad, Niu Changlei and Jin Hai-Bo 2015 *J. Appl. Phys.* **118** 14101
- [27] Nitin Kumar, Alok Shukla and Choudhary R N P 2017 *J. Mater. Sci.: Mater. Electron* **28(9)** 6673 <https://doi.org/10.1007/s10854-017-6359-y>
- [28] Jonscher A K 1996 *Universal Relaxation Law* (London: Chelsea Dielectrics Press)
- [29] Sujit Kumar, Dehury, Kalpana Parida and Choudhary R N P 2017 *J. Mater. Sci.: Mater. Electron.* <https://doi.org/10.1007/s10854-017-6816-7>
- [30] Hirose N and West A R 1996 *J. Am. Ceram. Soc.* **79** 1633
- [31] Pant M, Kanchan D K and Gondaliyam N 2009 *Mater. Chem. Phys.* **115** 98
- [32] Liu J, Duan C G, Yin W G, Mei W N, Smith R W and Hardy J R 2003 *J. Chem. Phys.* **119** 2812
- [33] Kamal M M and Bhuiyan A H 2014 *J. Mod. Sci. Tech.* **2** 1
- [34] Damjanovic D 1998 *Rep. Prog. Phys.* **61** 1267
- [35] Cai W, Zhong S X, Fu C L, Chen G and Deng X L 2014 *Mater. Res. Bull.* **50** 259